






Orthophosphate increases the efficiency of slow muscle-myosin isoform in the presence of omecamtiv mecarbil

Serena Governali^{1,2,4}, Marco Caremani ^{1,4}, Cristina Gallart¹, Irene Pertici ¹, Ger Stienen^{2,3}, Gabriella Piazzesi ¹, Coen Ottenheijm², Vincenzo Lombardi ¹✉ & Marco Linari ¹

Omecamtiv mecarbil (OM) is a putative positive inotropic tool for treatment of systolic heart dysfunction, based on the finding that in vivo it increases the ejection fraction and in vitro it prolongs the actin-bond life time of the cardiac and slow-skeletal muscle isoforms of myosin. OM action in situ, however, is still poorly understood as the enhanced Ca^{2+} -sensitivity of the myofilaments is at odds with the reduction of force and rate of force development observed at saturating Ca^{2+} . Here we show, by combining fast sarcomere-level mechanics and ATPase measurements in single slow demembranated fibres from rabbit soleus, that the depressant effect of OM on the force per attached motor is reversed, without effect on the ATPase rate, by physiological concentrations of inorganic phosphate (Pi) (1-10 mM). This mechanism could underpin an energetically efficient reduction of systolic tension cost in OM-treated patients, whenever [Pi] increases with heart-beat frequency.

¹PhysioLab, Department of Biology, University of Florence, Sesto Fiorentino 50019, Italy. ²Department of Physiology, Amsterdam UMC (location VUmc), 1081 HZ, Amsterdam, The Netherlands. ³Present address: Department of Physiology, Kilimanjaro Christian Medical University College, Moshi, Tanzania. ⁴These author contributed equally: Serena Governali, Marco Caremani. ✉email: vincenzo.lombardi@unifi.it

In the heart, mutations in the myosin motor are responsible for cardiomyopathies, which consist either in an increased contractility with reduced ventricular filling or diastolic dysfunction (hypertrophic cardiomyopathy, HCM) or in a decreased contractility with reduced ejection fraction or systolic dysfunction (dilated cardiomyopathy)¹. A promising approach for systolic dysfunction treatment is the development of small molecules that, acting as cardiac myosin activators, are able to increase the contractility during the systole. Among them, omecamtiv mecarbil (OM) has been found to increase the systolic ejection fraction^{2–6} and is currently in phase-three clinical trial⁷. OM acts on both α and β cardiac myosin heavy chain (MHC) isoforms and on the slow-skeletal MHC isoform⁸. Noteworthy, the β cardiac MHC isoform, which accounts for >95% of the myosin in the human ventricle, is encoded by the same gene (*MYH7*) as the slow-skeletal MHC isoform^{8–12} and the two isoforms will be named β /slow MHC hereafter. OM binds to the catalytic domain of the myosin molecule between the nucleotide binding pocket and the converter domain, a communicating zone between the active site and the lever arm responsible for the working stroke. As a consequence, the release of inorganic phosphate (Pi) is promoted and the lever arm of the molecular motor is stabilized in a pre-working stroke position^{2,13,14}. Accordingly, the velocity of actin sliding in the *in vitro* motility assay is reduced by OM^{15–17}. A recent *in vitro* mechanical study⁹ has significantly advanced the understanding of OM mechanism, showing that OM binding to β -cardiac myosin inhibits the working stroke and prolongs the actin-attachment life time of the motor. In this way, *in situ*, OM may increase thin filament activation at low Ca^{2+} allowing recruitment of OM-free motors, able to generate force. However, a detailed *in situ* analysis of the effects of OM on the mechanokinetics and energetic of myosin motors has still to be done.

Here we determine, in Ca^{2+} -activated demembrated fibres from rabbit soleus, the effects of OM on either the number and force of the attached myosin motors or their ATPase activity and how physiological concentrations of inorganic phosphate (Pi) influence these parameters. The slow-skeletal muscle of the rabbit has been chosen instead of the heart because their myosin isoforms exhibit similar affinity for OM⁸, while the required nanometre-microsecond resolution of sarcomere-level mechanics can only be achieved in demembrated myocytes from skeletal muscle^{18,19}. Intact trabeculae dissected from the ventricle of the rat heart, on which sarcomere-level mechanics has been recently successfully exploited^{20,21}, do not suit the present investigation because (i) only skinned myocytes allow the required manipulation of $[\text{Ca}^{2+}]$ and $[\text{Pi}]$ and (ii), only ~20% of the myosin is β /slow MHC isoform and the remaining ~80% is α MHC isoform²¹. Determining the fraction of motors recruited for actin interaction during Ca^{2+} -activated isometric contraction of demembrated soleus fibres allowed the demonstration that OM reduces the average force per attached motor but at low Ca^{2+} it increases the number of attached motors. The inhibitory effect of OM on force generation is reversed by increasing $[\text{Pi}]$ (range 1–10 mM), which acts as an allosteric competitor that allows the OM-bound no-force-generating motors to release OM and re-enter the force-generating cycle without any change in the rate of ATP hydrolysis. We conclude that in the heart systole, in which the internal $[\text{Ca}^{2+}]$ remains below the saturating level, the inotropic action of OM occurs via two mechanisms: the first is the increase in the number of attached motors, the second, emerging at physiological levels of intracellular Pi (1–10 mM^{22–28}), is a Pi-dependent recovery of the force per motor. This effect of Pi on the OM-bound motors represents an energetically efficient inotropic response in patients under OM treatment, whenever the increase of heart-beat frequency increases $[\text{Pi}]$ ^{27,28}.

Results

Titration of OM effect on the isometric force development. Following a temperature jump from 1 to 12 °C in the activating solution at saturating $[\text{Ca}^{2+}]$ (pCa 4.5), the force rises from near zero to a steady value (T_0) with an almost exponential time course (Fig. 1a). Addition of 1 μM OM halves T_0 and slows the force development that shows a sigmoidal shape (Fig. 1b). In eight fibres T_0 decreases from 146 ± 5 kPa in the control to 64 ± 3 kPa in the presence of 1 μM OM. The reciprocal of the half-time for force development, r_{TD} , taken as an estimate of the rate of force development, is reduced by 1 μM OM from 3.7 ± 0.2 s⁻¹ to 1.9 ± 0.1 s⁻¹. The reduction of both T_0 and r_{TD} by OM is dose-dependent as shown by the relations of T_0 (Fig. 1c) and r_{TD} (d) versus $[\text{OM}]$. The effect nearly saturates at 10 μM OM when T_0 is ~35 kPa and r_{TD} is ~1.4 s⁻¹. The concentration of OM for half-maximal effect is ~0.5 μM for both T_0 and r_{TD} .

OM does not alter the fraction of motors at full activation. The half-sarcomere stiffness at T_0 (k_0) during maximal Ca^{2+} activation is estimated from the slope of the T_1 relation determined, both in the control and in the presence of OM (range 0.1–10 μM), by plotting the force attained in response to stepwise changes in fibre length against the corresponding changes in the half-sarcomere length measured with the striation follower (see “Methods”) (Fig. 2a, b). The T_1 relations are shown in Fig. 2c in both control (filled circles) and 1 μM OM (open circles). Both the ordinate intercept (T_0) and the abscissa intercept (Y_0 , an estimate of the half-sarcomere strain at T_0) reduce in OM (open circles) by a similar amount (~60%) relative to the control (filled circles). Thus, the slope of the T_1 relation, k_0 , is the same in the presence of OM as in control. In the eight fibres used for these experiments, k_0 is 28.1 ± 0.7 kPa nm⁻¹ in control and remains almost constant independent of $[\text{OM}]$ in the whole range of concentrations used (0.1–10 μM , Fig. 2d, triangles), with a mean value of 29.8 ± 0.6 kPa nm⁻¹ (dashed line). In the same range of $[\text{OM}]$, Y_0 linearly depends on the isometric force and the extrapolation of the relation to zero force crosses the origin (Fig. 2e). This result indicates that the reduction of isometric force by OM at saturating $[\text{Ca}^{2+}]$ is due to a proportional reduction in the strain of all the elastic elements in the half-sarcomere (myofilaments and attached myosin motors) and thus OM reduces the half-sarcomere force by reducing the average force per attached myosin motor without changing the number of attached motors.

This conclusion is supported quantitatively by extracting the stiffness of the array of attached motors, e_0 (Fig. 2f), from k_0 . e_0 is determined by subtracting the contribution of the filament compliance (C_f) from the half-sarcomere compliance (see “Methods”). The procedure is based on the definition of the half-sarcomere in terms of a simple mechanical model in which the attached motors, represented by an array of in parallel springs with average strain s_0 ¹⁸, are in series with the actin and myosin filament elasticity represented by a spring with an equivalent filament compliance C_f . The values of C_f and s_0 are reported in Table 1. Knowing C_f (15.2 nm MPa⁻¹, average from Table 1), the dependence of e_0 on $[\text{OM}]$ can be calculated from the relation between k_0 and $[\text{OM}]$ (Eq. (1)). As shown in Fig. 2f, e_0 remains almost constant (~55 kPa nm⁻¹) independent of $[\text{OM}]$. Under the sensible assumption that OM does not affect the stiffness of the motor, e_0 is an estimate of the fraction of attached motors, β , which results constant independent of $[\text{OM}]$. On the other hand, in the presence of 1 μM OM s_0 decreases from 3.20 to 1.57 nm (Table 1), indicating that the reduction of T_0 to ~1/2 by 1 μM OM (Fig. 1c) is fully accounted for by a corresponding decrease in s_0 . T_0 and the strain of all the elastic elements decrease in proportion in the whole range of $[\text{OM}]$ (Fig. 2e), indicating that

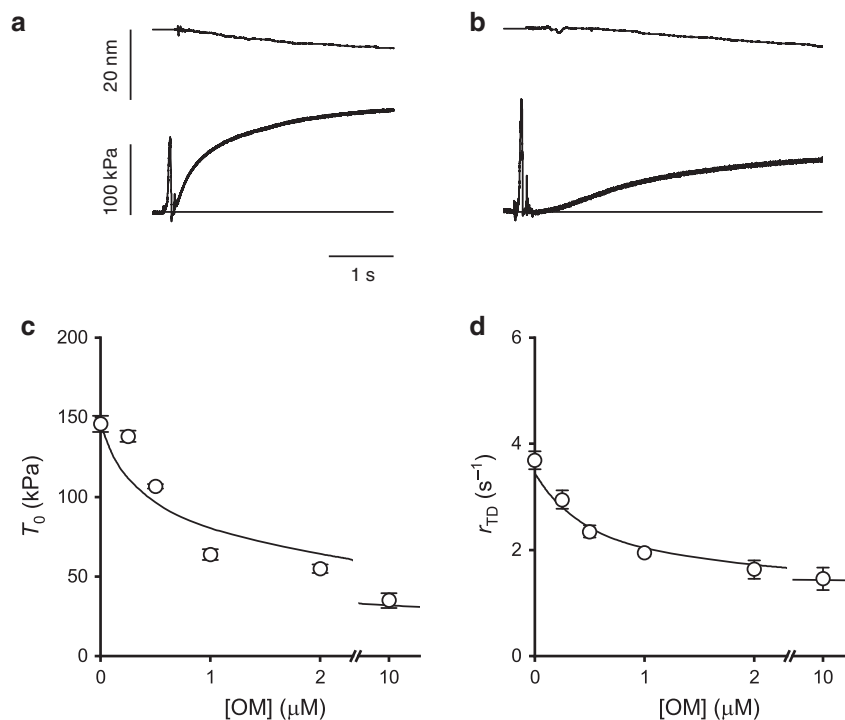


Fig. 1 Effect of OM on isometric force development. Force development following T-jump (from 1 to 12 °C) in control (a) and in the presence of 1 μM OM (b) on an activated fibre (pCa 4.5). Traces show the length change per half-sarcomere (upper trace) and the force (lower trace). The artefact in the traces marks the transition to the test temperature drop. The horizontal line in the lower panels indicates zero force. Fibre length, 4.5 mm; length of the segment under the striation follower, 0.8 mm; average sarcomere length within the segment, 2.3 μm; CSA, 3000 μm²; pCa, 4.5. Dependence of the isometric force T_0 (c) and of the rate of force development r_{TD} (d) on the concentration of OM. Lines, simulation with model of Fig. 6. Data are mean values \pm SEM from eight fibres. Source data are provided as a Source Data file.

the reduction of s_0 accounts for that in T_0 . The average force per attached motor (F_0) can be calculated from s_0 if the stiffness of the myosin motor (ϵ) is known: $F_0 = s_0 \cdot \epsilon$. Taking ϵ for the slow myosin isoform = 0.56 ± 0.04 pN nm⁻¹¹⁹, F_0 is 1.8 ± 0.2 pN in control and 0.9 ± 0.1 pN in 1 μM OM (Fig. 3c).

OM increases myofilament Ca-sensitivity for motor attachment. As $[Ca^{2+}]$ decreases, the depressant effect of OM on T_0 also decreases. As shown in Fig. 3a, at pCa between 4.5 and 6.5, T_0 is lower in OM (open circles) than in control (filled circles), while at pCa > 7 T_0 is higher in OM. Fitting the data with the Hill equation shows that pCa₅₀ (the pCa at which force attains half-maximum) increases from 6.57 in the control (continuous line) to 7.02 in the presence of OM (dashed line) (Table 2), indicating a corresponding increase in Ca²⁺-sensitivity of the force. At the same time the slope of the relation, estimated by the parameter n of the Hill equation, which is an indicator of the degree of cooperativity in myofilament activation, decreases from 2.01 in the control to 0.84 in the presence of OM.

The stiffness of the array of attached motors e_0 (an estimate of β) and the average motor strain s_0 at each pCa can be calculated both in control and in 1 μM OM using Eqs. (1) and (2) as detailed in “Methods”. As shown in Fig. 3b, while at saturating $[Ca^{2+}]$ e_0 is the same with and without OM, at pCa larger than ~6.5 e_0 is higher in OM (open circles) than in control (filled circles). Instead the strain per motor s_0 and thus the force per motor F_0 are halved by the addition of 1 μM OM at saturating Ca²⁺ (pCa 4.5) (Fig. 3c), but are not affected by the reduction of $[Ca^{2+}]$ in either the absence (filled circles) or the presence of OM (open circles).

The larger value of β in OM at sub-saturating $[Ca^{2+}]$ but not at saturating $[Ca^{2+}]$ is the sign of a higher Ca²⁺ sensitivity, which

underpins OM as a potentiator of contractility^{8,29,30}. A more precise definition of the Ca²⁺ dependence of this effect is given in Fig. 3d, where the difference (ΔT_0) between the fitted T_0 -pCa relations in 1 μM OM (dashed line in Fig. 3a) and in control (continuous line) is plotted versus pCa. At pCa 6.8, the reduced average force per motor (~½) in 1 μM OM is compensated by the increased fraction of attached motors (~twice); at pCa > 6.8, 1 μM OM acts as a potentiator increasing the sarcomere force, because, while the force per motor is halved by 1 μM OM, the increased Ca-sensitivity gives a β larger than twice the control.

Effect of Pi on isometric contraction with and without OM.

The allosteric competition between binding of OM and the presence of Pi in the catalytic site^{2,13,14} of the motor has been studied by determining how, at pCa 4.5, the increase of [Pi] (range 1–30 mM, where 1 mM is the [Pi] assumed for the experiments without added Pi³¹) influences the effects of addition of OM on the relevant mechanical parameters of the contraction, T_0 , r_{TD} , e_0 (and thus β) and s_0 (and thus F_0). In control the increase in [Pi] decreases T_0 in a dose-dependent manner (Fig. 4a, filled circles) from 156 ± 1 kPa in control to 83 ± 1 kPa (–47%) in 30 mM Pi, with a [Pi] for half-maximum effect (EP_{i50}) of 8 mM. This effect is comparable with that reported in previous papers^{23,32,33}. Surprisingly, in 1 μM OM (Fig. 4a, open circles), T_0 (77 ± 4 kPa in no added Pi, in these experiments) remains almost constant for Pi < 10 mM and attains a value of 55 ± 1 kPa (–30%) in 30 mM Pi. r_{TD} in control (Fig. 4b, filled circles) is 3.8 ± 0.2 s⁻¹ without added Pi (in agreement with the ordinate intercept in Fig. 1d) and increases with the increase in [Pi] with a slope that progressively decreases. A similar Pi dependence of r_{TD} is observed in the relation determined in 1 μM OM (Fig. 4b, open circles), beyond the depressant effect reported in Fig. 1d.

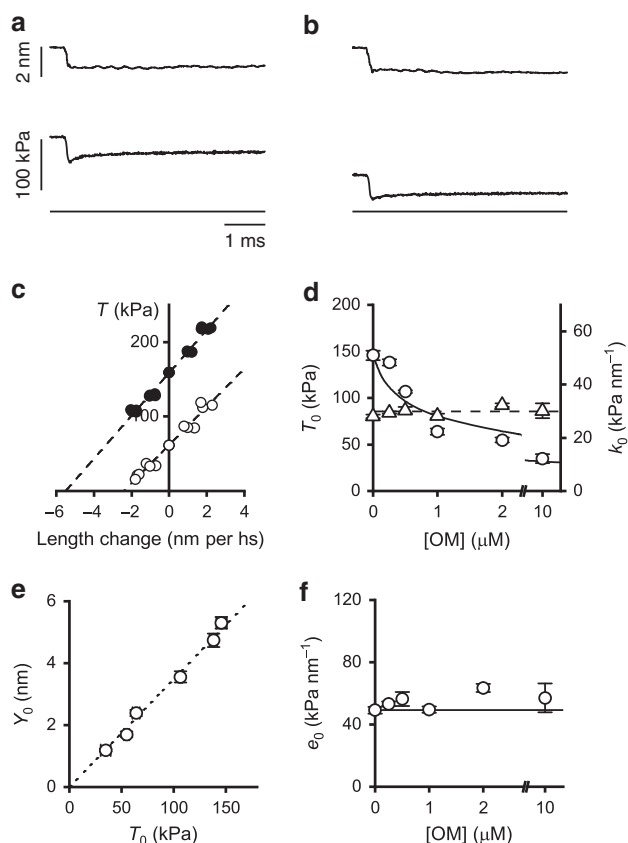


Fig. 2 Effect of OM on the relevant mechanical parameters determined by stiffness measurements. Sample records of the force response (middle trace) to a step length change (upper trace) imposed at the isometric plateau of an activated fibre (pCa 4.5) in control (**a**) and in the presence of 1 μM OM (**b**). Lower traces indicate zero force. **c** T_1 relations in control (filled circles) and in the presence of 1 μM OM (open circles) from the same fibre as (**a**) and (**b**). Dashed lines are 1st order regression equations fitted to the data. Same fibre as in Fig. 1. **d** Dependence of T_0 (left ordinate, circles) and half-sarcomere stiffness (right ordinate, triangles) on the concentration of OM. Circles are the same data as in Fig. 1c. Continuous line, model simulation of T_0 -[OM] relation; dashed line, mean value of k_0 in the whole range of OM concentrations. **e** Dependence of half-sarcomere strain (Y_0) on OM-modulated isometric force (T_0). Dotted line, linear regression on data points. **f** Dependence of cross-bridge stiffness (e_0) on the concentration of OM. Continuous line, value in the absence of OM. Data points in **d-f** are mean values \pm SEM from eight fibres. Source data are provided as a Source Data file.

In these experiments, e_0 without added Pi ($e_{0,1}$), calculated from the half-sarcomere stiffness k_0 (see Supplementary Note 1), is $54.2 \pm 4.4 \text{ kPa nm}^{-1}$ and $57.5 \pm 7.4 \text{ kPa nm}^{-1}$ without and with OM, respectively, in agreement with Fig. 2f. e_0 decreases with the increase in [Pi] with a slope that progressively reduces in almost the same way without (Fig. 4c, filled circles) and with OM (open circles), attaining $\sim 50\%$ the value without added Pi at 30 mM Pi. Thus, in the absence of OM, e_0 (and thus β) reduces with [Pi] almost in proportion to the reduction of T_0 (filled circles in Fig. 4a), indicating, in accordance with previous work in skinned fibres from fast skeletal muscle³⁴, that Pi reduces T_0 by reducing β without change in motor strain s_0 . In these Pi experiments s_0 (calculated with Eq. (2) from data as in Supplementary Fig. 1) is $3.08 \pm 0.19 \text{ nm}$ in the absence of OM (filled circles in Fig. 4d, left ordinate). Consequently, F_0 ($= s_0 \cdot \epsilon$) is $1.75 \pm 0.13 \text{ pN}$, independent of [Pi] (right ordinate in Fig. 4d, filled circles).

Table 1 Estimates of the mechanical parameters of the half-sarcomere.

	Control	1 μM OM
$T_{0,4.5}$ (kPa)	156 ± 7	69 ± 5
C_f (nm MPa $^{-1}$)	15.2 ± 1.3	15.3 ± 2.0
s_0 (nm)	3.20 ± 0.15	1.57 ± 0.10

C_f and s_0 are determined according to the procedure detailed in "Methods", in control and in the presence of OM. The isometric force at saturating Ca^{2+} is reported in the first row. $T_{0,4.5}$, mean \pm SEM from four fibres. C_f and s_0 , slope and ordinate intercept from data in Fig. 7c. Source data are provided as a Source Data file.

Table 2 Parameters of Hill's equation fit to force-pCa relation in control and in the presence of OM.

	Control	1 μM OM
n	2.01 ± 0.14	0.84 ± 0.15
pCa $_{50}$	6.57 ± 0.01	7.02 ± 0.07

n estimates the slope of the relation, pCa $_{50}$ (the pCa at which force attains half-maximum) estimates the Ca^{2+} sensitivity. Data are mean \pm SEM from four fibres. Data from Fig. 3a.

In the presence of 1 μM OM, the lack of the inhibitory effect of the increase in Pi on T_0 for [Pi] < 10 mM (Fig. 4a, open circles), while β decreases in the same way as in control (-38% at 10 mM Pi, Fig. 4c), results in the increase of the average motor strain s_0 from $1.41 \pm 0.15 \text{ nm}$ to $2.06 \pm 0.06 \text{ nm}$ (+46%, left ordinate in Fig. 4d, open circles). Above 10 mM, Pi induces, also in the presence of 1 μM OM, comparable reduction of both T_0 and e_0 (open circles in Fig. 4a and c), so that s_0 remains roughly constant (open circles in Fig. 4d). F_0 increases from 0.79 ± 0.10 to $1.16 \pm 0.09 \text{ pN}$ with the increase in [Pi] in the range 1–10 mM (right ordinate in Fig. 4d, open circles) and then, for [Pi] > 10 mM, remains roughly constant at $\sim 1.1 \text{ pN}$, a value that anyway is still lower than in the absence of OM ($\sim 1.7 \text{ pN}$).

OM and the rate of ATP hydrolysis in isometric contraction.

Faced with the contradictory or not exhaustive results on the OM effects on the ATPase activity^{2,15,29,35}, the effect of the increase in [Pi] (range 1–20 mM) on the ATP hydrolysis rate (k_{cat}) in isometric contraction has been determined in the absence and in the presence of OM (Fig. 5a, b). In these experiments, in agreement with the mechanical experiments, in solution with no added Pi T_0 is reduced to $\sim 50\%$ the control value by the addition of 1 μM OM (circles in Fig. 5b). k_{cat} , instead, does not change significantly (triangles), being $0.055 \pm 0.007 \text{ mM s}^{-1}$ in the absence of OM and $0.055 \pm 0.005 \text{ mM s}^{-1}$ and $0.052 \pm 0.006 \text{ mM s}^{-1}$ in 1 μM and 2 μM OM, respectively.

Effect of Pi on ATP hydrolysis rate with and without OM.

The increase of [Pi] in the absence of OM reduces by the same amount T_0 (Fig. 5c, filled circles, data similar to those in Fig. 4a) and k_{cat} (Fig. 5d, filled circles). This finding is in agreement with previous work³⁶. In the presence of 1 μM OM, the increase in [Pi] has an inhibitory effect on T_0 that emerges only at [Pi] above 10 mM (Fig. 5c, open circles, data similar to those in Fig. 4a, open circles). Instead, k_{cat} is reduced by the increase in [Pi] (Fig. 5d, open circles) in the same way as in the absence of OM (filled circles). The tension cost of the isometric contraction (E_T) can be calculated as the ratio of k_{cat} over T_0 (Fig. 5e). Without added Pi, E_T in the presence of 1 μM OM is almost twice the control (points at 1 mM Pi in Fig. 5e, filled circle control, open circle 1 μM OM), as a consequence of the depressant effect of OM on the force per

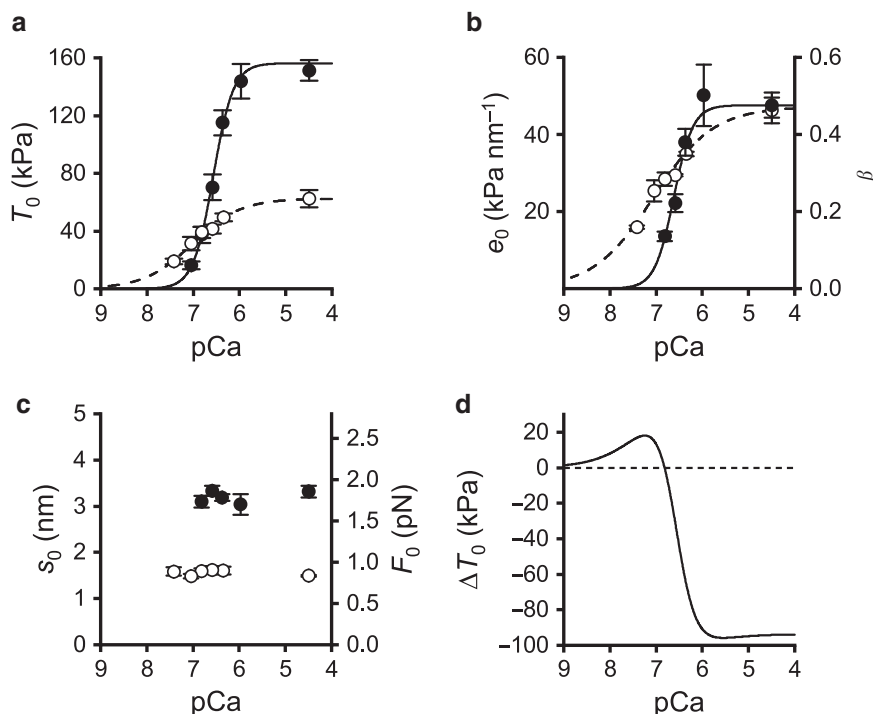


Fig. 3 Effect of OM on myofilament Ca^{2+} sensitivity for motor attachment. **a** T_0 -pCa relation in control (filled circles) and in the presence of $1\ \mu\text{M}$ OM (open circles). Continuous (control) and dashed ($1\ \mu\text{M}$ OM) lines are calculated by fitting Hill equation $T_0 = T_{0,45} / (1 + 10^{n(\text{pCa} - \text{pCa}_{50})})$ to data. The best fit parameters are listed in Table 2. **b** Dependence of the stiffness of the motor array (e_0 , left ordinate) and of the fraction of attached motors (β , right ordinate) on $[\text{Ca}^{2+}]$. β in control at saturating $[\text{Ca}^{2+}]$ is assumed 0.47¹⁹. Continuous (control) and dashed ($1\ \mu\text{M}$ OM) lines are calculated by fitting the Hill's sigmoidal equation to data. **c** Dependence of the strain per motor (s_0 , left ordinate) and of the force per motor (F_0 , right ordinate) on $[\text{Ca}^{2+}]$. **d** Dependence of the difference (ΔT_0) between the fitted T_0 -pCa relation in $1\ \mu\text{M}$ OM (dashed line in **a**) and in control (continuous line in **a**) on $[\text{Ca}^{2+}]$; dashed line indicates zero difference. In all panels, $[\text{Ca}^{2+}]$ is expressed in pCa units. Data in **a-c** are mean values \pm SEM from four fibres. Source data are provided as a Source Data file.

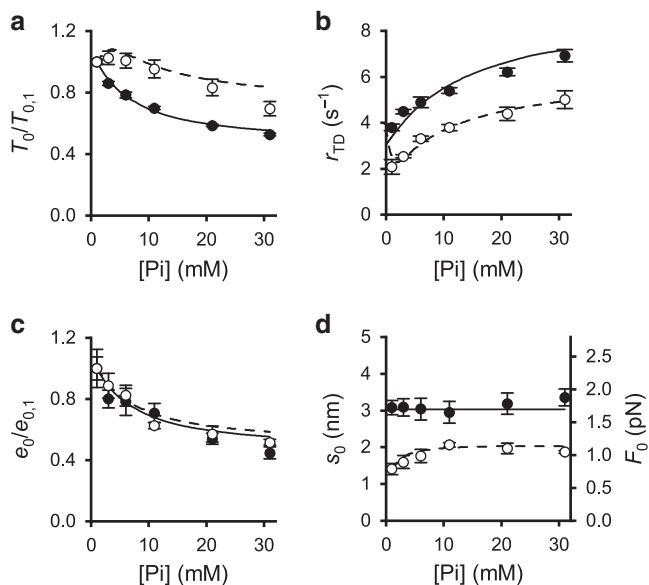


Fig. 4 Effect of Pi on the isometric mechanical parameters with and without OM. Filled circles and continuous lines, control; open circles and dashed lines, in the presence of $1\ \mu\text{M}$ OM. **a** Pi dependence of the isometric force (T_0) expressed in units relative to the value without added Pi ($T_{0,1}$). **b** Rate of force development (r_{TD}). **c** Stiffness of the motor array (e_0) relative to the value without added Pi ($e_{0,1}$). **d** Motor strain (s_0 , left ordinate) and motor force (F_0 , right ordinate). In each panel: symbols, experimental data; lines, model simulation. Data are mean values \pm SEM from three fibres. Source data are provided as a Source Data file.

motor F_0 without effect on k_{cat} . In the absence of OM E_T remains the same independent of $[\text{Pi}]$ (filled circles), while in $1\ \mu\text{M}$ OM (open circles) E_T decreases with the increase of $[\text{Pi}]$ approaching the value in the absence of OM.

Model simulation. A kinetic model able to explain the effects of OM and Pi on the in situ mechanics and energetics of the β /slow MHC isoform of myosin has been developed. The model is based on that originally proposed for fast skeletal muscle fibres from rabbit psoas^{34,37}, which has been modified to adapt the rate constants of the forward and backward transitions and the corresponding equilibrium constants (k_{+x} , k_{-x} and K_x , respectively) to fit the bulk of kinetic data from in vitro and in situ studies of β /slow MHC isoform in control condition (without added Pi and OM)^{9,15,32,38} (see Table 3 for the detailed justification of the assumptions made for each kinetic step and the dedicated section in Methods for the criteria of selection of the parameters for the model fitting). In particular, relevant kinetic constraints in this study are as follows: (i) $r_{\text{TD}} \sim 4\ \text{s}^{-1}$ (Fig. 1d, ten times slower than that of fast muscle), (ii) β at $T_0 = 0.47$ (40% larger than that of fast muscle¹⁹) and (iii) $k_{\text{cat}} = 0.055\ \text{mM}^{-1}\ \text{s}^{-1}$ (ten times slower than that of fast muscle³⁹). The original model³⁷ (green-highlighted part of the scheme in Fig. 6), in agreement with experimental evidence^{34,39-44}, assumes the formation of strongly bound, force-generating motors also before Pi release, so that rise in Pi should exert a minor inhibitory effect on T_0 and β than on k_{cat} . In contrast to this view, in fast skeletal muscle fibres Pi reduces T_0 and β more than k_{cat} ^{34,39}, suggesting that the conventional chemo-mechanical cycle has to be integrated with a branch that allows motor detachment at an early stage of the

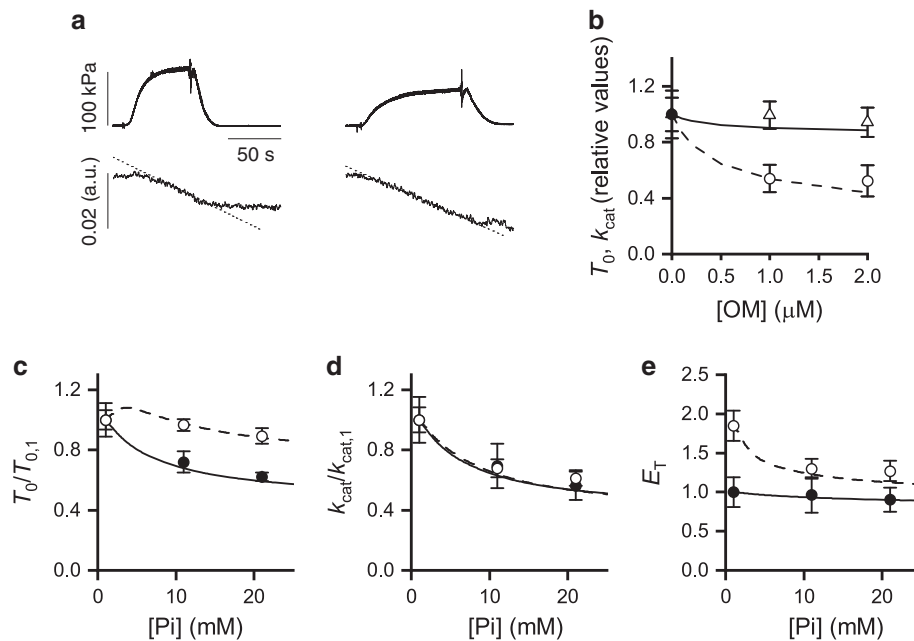


Fig. 5 Effect of OM on the rate of ATP hydrolysis in isometric contraction and its modulation by Pi. **a** Sample records from an activated fibre (pCa 4.5) of the time course of force and light absorbance (in absorbance units, a.u.) in the absence (left) and in the presence (right) of 1 μM OM. The dotted line on the absorbance trace is the 1st order regression equation fitted to the trace after force has attained a steady value. The slope of the regression is used as a measure of the ATP hydrolysis rate (k_{cat}). **b** Dependence on OM of T_0 (circles and dashed line) and k_{cat} (triangles and continuous line). Values are relative to the isometric values in the absence of OM (98 ± 17 kPa and 0.055 ± 0.007 mM s^{-1} , respectively). **c** Dependence on Pi of the isometric force (T_0) relative to the value without added Pi ($T_{0,1}$) in the absence (filled circles and continuous line) and in the presence (open circles and dashed line) of 1 μM OM. **d** Dependence on Pi of k_{cat} relative to the value without added Pi ($k_{\text{cat},1}$). Symbols and lines as in (c). **e** Tension cost of the isometric contraction (E_T). Symbols and lines as in (c). E_T is normalized by the value in the absence of OM and no added Pi. **b–e** symbols, experimental data; lines, model simulation. Data are mean values \pm SEM from 12 fibres in (b) and from four fibres in (c–e). Source data are provided as a Source Data file.

ATPase cycle (step 6), with Pi still bound to the catalytic site. The finding in this work that β and k_{cat} are reduced by the same extent by the rise in Pi (filled circles in Figs. 4c and 5d) confirms the requirements for the unconventional early detachment with the hydrolysis products still bound to the catalytic site.

To explain the effects of OM on the mechano-kinetics of the β /slow isoform of the myosin motor in situ a branched pathway (pink-highlighted part in the scheme of Fig. 6) is required. In this way the scheme accounts for both the features present in the literature (points *i*, *ii* below) and those reported in this work (points *iii–v* below): (i) OM binds to the catalytic domain of the myosin motor in the conformation at the beginning of the working stroke (step 8) and increases the probability of its attachment to actin (step 9), accelerating the release of Pi (step 10) and preventing the working stroke and the force generation^{2,9,13–15}; (ii) OM-ADP motors detach by a process that does not imply ATP binding (step 12)⁹; (iii) strongly bound force-generating motors and attached OM-bound motors have the same stiffness, to account for the lack of effect of OM on k_0 (Fig. 2d, triangles and dashed line) and e_0 (Fig. 2f); (iv) the $\text{AM}'_{\text{OM}}\text{-ADP}$ state generated after Pi release (step 10) undergoes an isomerization (step 11) to a new state ($\text{AM}''_{\text{OM}}\text{-ADP}$) with increased affinity for Pi and thus at $[\text{Pi}] > 0$ (also without added Pi, when contaminating $[\text{Pi}]$ is 1 mM) can rebound Pi, release OM and re-enter the force-generating cycle (step 14); in this way, by appropriate selection of the kinetics of steps 11 and 14 (Table 3), the model is able to account for both the OM-dependent reduction in r_{TD} at any $[\text{Pi}] > 0$ (Fig. 1d, continuous line and Fig. 4b), and the Pi-dependent increase in F_0 in 1 μM OM (Fig. 4d, open circles); (v) the rate limiting step in isometric contraction, that in the conventional cycle is the ADP release (step 5), in the OM cycle is detachment (step 12). Thus k_{+12} is set

$\cong k_{+5}$, to account for the finding that k_{cat} is not affected by $[\text{OM}]$ (Fig. 5b triangles) and is reduced by the increase in Pi in the same way in the absence as in the presence of OM (Fig. 5d).

In the presence of OM the probability for an M-ADP-Pi motor to escape the conventional cycle (green pathway in Fig. 6) by binding OM and entering the pink pathway (step 8) is controlled by the second-order equilibrium constant K_8 , which is set at a value $4 \cdot 10^6$ M^{-1} (Table 3) in order to fit the force— $[\text{OM}]$ relation of Fig. 1 (continuous line). The kinetics of steps 11, the isomerization that changes Pi affinity of the OM-bound motor, and step 14, in which Pi competes with OM for binding to the attached motor after the isomerization step (step 11), are dictated by the following constraints: (i) without added Pi ($[\text{Pi}] \sim 1$ mM) and in the presence of OM, r_{TD} attains the minimum value $\sim 1/2$ the control with a $[\text{OM}]_{50} = 0.5$ μM (Fig. 1d); (ii) increase in $[\text{Pi}]$ reduces β in the same way in the absence and presence of OM (Fig. 4c); (iii) in 1 μM OM the force per motor increases by 50% with the increase of $[\text{Pi}]$ in the range 1–10 mM (Fig. 4d). These results are fitted (dashed line) assuming, for step 11 an equilibrium constant (K_{11}) = 1, and for step 14, a second-order rate constant for Pi binding (k_{+14}) = $3 \cdot 10^3$ $\text{M}^{-1} \text{s}^{-1}$ and a second-order rate constant for OM binding (k_{-14}) = $3 \cdot 10^6$ $\text{M}^{-1} \text{s}^{-1}$ (Table 3).

Discussion

Sarcomere-level mechanics of demembrated fibres from rabbit soleus muscle allow a double mechanism of OM action on the β /slow MHC isoform to be revealed, which eventually accounts for a Pi-dependent recovery of efficiency of the contractile response of OM-treated fibres.

The first mechanism of action, which confirms the conclusions of recent work *in vitro*^{9,14}, implies a dose-dependent depression

Table 3 Rate constants for the forward (k_{+x}) and backward (k_{-x}) transitions and corresponding equilibrium constants (K_x) for the scheme of Fig. 6.

Step in the cycle	k_{+x}	k_{-x}	K_x	Justification
A, green-highlighted path in Fig. 6				
(1)	$1 \times 10^6 \text{ M}^{-1}\text{s}^{-1}$	1 s^{-1}	$1 \times 10^6 \text{ M}^{-1}$	According to refs. 32,38,62,63
(2)	14 s^{-1}	9 s^{-1}	1.56	k_{+2} , according to ref. 38; k_{-2} , selected to adjust the distribution of detached myosin motors
(3)	2.2 s^{-1}	4.5 s^{-1}	0.49	k_{+3} , adjusted to fit the fraction of attached motors in isometric contraction ¹⁹
(4)	11 s^{-1}	$0.9 \times 10^3 \text{ M}^{-1}\text{s}^{-1}$	$12.2 \times 10^{-3} \text{ M}$	k_{+4} from refs. 9,15 (assuming $Q_{10} = 2$) and K_4 adjusted to fit the Pi dependence of the rate of force development assuming these steps are 50 times slower than in psoas muscle ³²
(5)	1 s^{-1}	$1 \times 10^3 \text{ M}^{-1} \text{ s}^{-1}$	$1 \times 10^{-3} \text{ M}$	Adjusted to fit k_{cat} in isometric contraction in the absence of OM ⁶⁴⁻⁶⁶
(6)	0.8 s^{-1}	$2 \times 10^{-3} \text{ s}^{-1}$	0.4×10^3	Adjusted to fit the Pi dependence of k_{cat} in the absence of OM ³⁷
(7)	50 s^{-1}	-	-	Rapid and irreversible release of hydrolysis products and ATP binding ³⁷
B, pink-highlighted path in Fig. 6				
(8)	$400 \times 10^6 \text{ M}^{-1}\text{s}^{-1}$	100 s^{-1}	$4 \times 10^6 \text{ M}^{-1}$	Adjusted to have the correct proportion of OM-bound myosin motors
(9)	1.2 s^{-1}	1 s^{-1}	1.2	k_{+9} and k_{-9} adjusted to account for OM-dependent increase of probability of actin attachment by motors ($K_9 > K_3$) ¹⁵ and for the constant total number of attached motors in the presence of OM
(10)	18 s^{-1}	$1.48 \times 10^3 \text{ M}^{-1} \text{ s}^{-1}$	$12.2 \times 10^{-3} \text{ M}$	k_{+10} set to $1.64 k_{+4}$, to take into account the effect of OM on the rate of Pi release ^{9,15} ; K_{10} , same value as in step (4)
(11)	1000 s^{-1}	1000 s^{-1}	1	Rapid isomerization step; K_{11} set to 1 to adjust the stoichiometry of the Pi effect
(12)	1.5 s^{-1}	$2 \times 10^{-3} \text{ s}^{-1}$	1×10^3	Detachment set to fit k_{cat} in the presence of OM
(13)	3 s^{-1}	-	-	Irreversible release of ADP and OM followed by rapid ATP binding
(14)	$3 \times 10^3 \text{ M}^{-1}\text{s}^{-1}$	$3 \times 10^6 \text{ M}^{-1}\text{s}^{-1}$	1×10^{-3}	Adjusted to fit the kinetics of force development and the Pi dependence of T_D and e_0 in the presence of OM

Values for the model in the absence of OM (A, green-highlighted in Fig. 6) and for the branched pathway induced by OM (B, pink-highlighted in Fig. 6). The justification of the kinetic parameters are reported in the last column. Where possible, the parameters are selected according to the relevant information from the literature. The selection of the value of the kinetic parameters concerning OM and OM-Pi actions and the sensitivity of the model fit to the selected value are achieved with an iterative procedure of model simulation by changing one parameter at a time as detailed in "Methods" and in Supplementary Figs. 2 and 3. x represents the step number, as reported in brackets in the first column. For the second-order rate constants, the apparent rate constants are calculated assuming $[\text{MgATP}] = 5 \text{ mM}$ and $[\text{ADP}] = 20 \text{ }\mu\text{M}$; $[\text{Pi}]$ and $[\text{OM}]$ according to the experimental conditions.

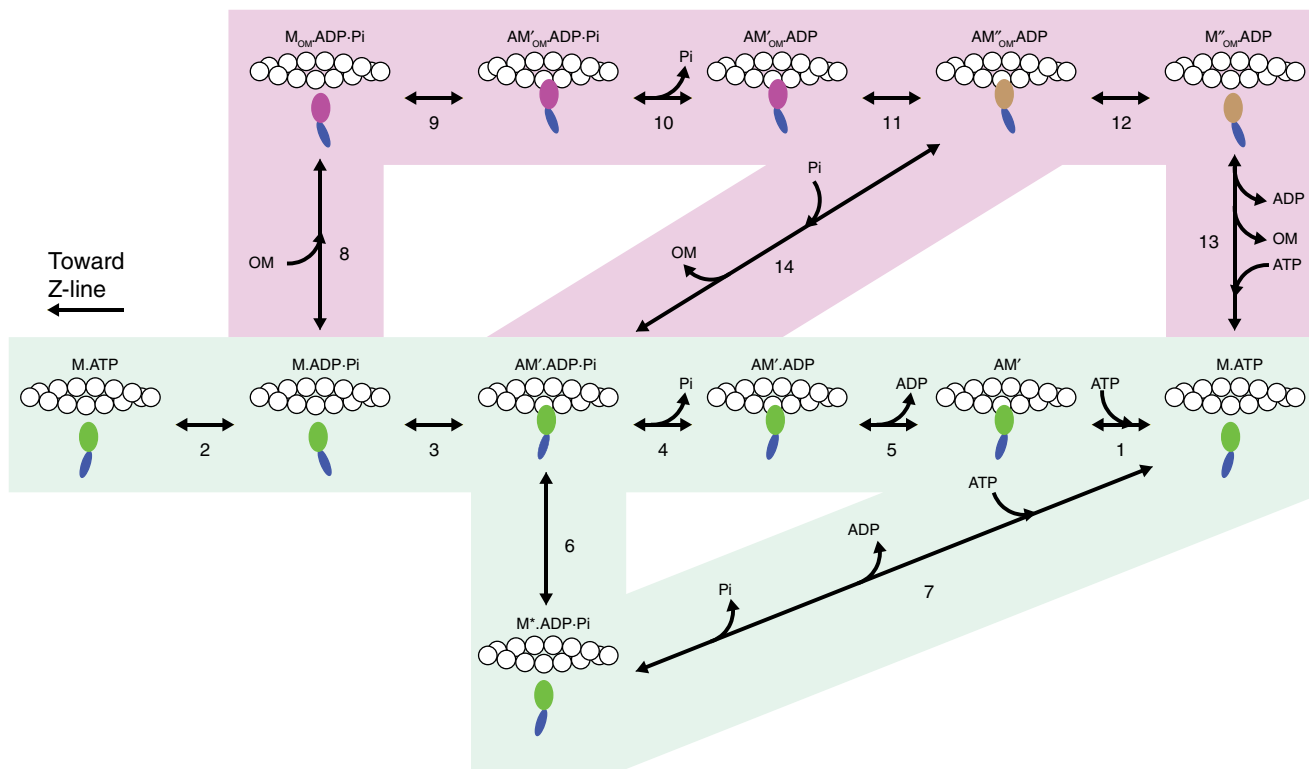


Fig. 6 Chemo-mechanical cycle of the myosin motor. The green-highlighted part is the original model³⁷; the pink-highlighted part is the branched pathway promoted by OM. Myosin catalytic domain is green for the motors without OM (M) and magenta and brown for the OM-bound motors (M_{OM}) before and after the isomerization step (step 11), respectively. The working stroke in the attached head is indicated by the tilting of the light chain domain (the lever arm, blue) towards the Z-line. The system of linear differential equation for the calculation of state transitions is reported in Supplementary Note 2.

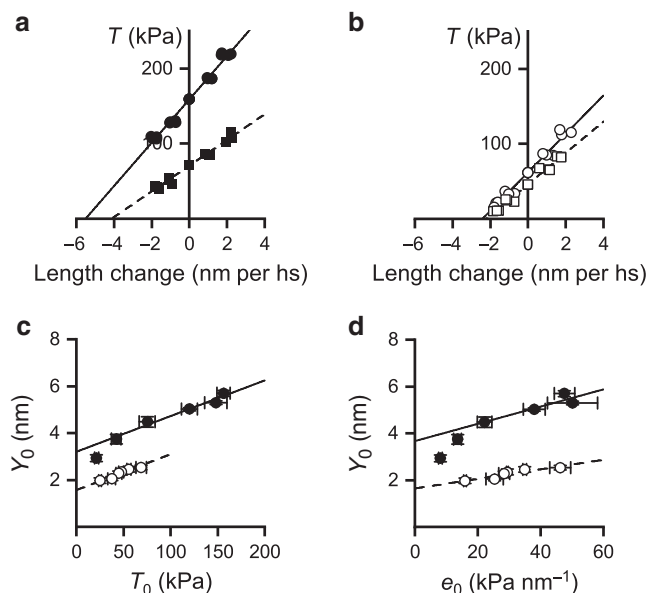


Fig. 7 Estimate of myofilament compliance and motor strain. T_1 relations from a fibre in control (**a**) and in the presence of $1\ \mu\text{M}$ OM (**b**) at pCa 4.5 (circles) and 6.59 (squares). The relations are obtained by plotting the extreme force attained at the end of the length step, T_1 , versus the step size. Lines in **a** and **b** are 1st order regression equations fitted to the data (pCa 4.5, continuous; pCa 6.59, dashed). The abscissa intercept of each line is the average strain of the half-sarcomere before the length step (Y_0). Fibre length, 4.2 mm; segment length under the striation follower, 0.77 mm, average segment sarcomere length, $2.34\ \mu\text{m}$, test temperature, $12.2\ ^\circ\text{C}$. **c** Relations of Y_0 versus T_0 at different pCa determined in control (filled circles) and in the presence of $1\ \mu\text{M}$ OM (open circles); mean values \pm SEM from four fibres. The lines are linear regressions on the pooled data for forces $>30\ \text{kPa}$ in control (continuous) and in the presence of OM (dashed). The slope and the ordinate intercept of the linear regressions are listed in Table 1. **d** Relations of half-sarcomere strain (Y_0) versus the stiffness of the myosin motors at different pCa (e_0) in control (filled circles) and in the presence of $1\ \mu\text{M}$ OM (open circles); mean values \pm SEM from four fibres. The lines are linear regressions on the pooled data for stiffness $>20\ \text{kPa}\ \text{nm}^{-1}$ in control (continuous) and in the presence of OM (dashed). **c** and **d**, data from four fibres. Source data are provided as a Source Data file.

of the active sarcomere force by OM binding to the myosin motor in the pre-working stroke state that promotes an unconventional cycle in which the working stroke is prevented and the detachment occurs without binding of ATP.

We find that, irrespective of $[\text{Ca}^{2+}]$, in $1\ \mu\text{M}$ OM the fraction of OM-bound attached motors is $\sim 50\%$ of the total (β), as indicated by the average force per motor, F_0 , that remains $\sim 50\%$ of that in control at any $[\text{Ca}^{2+}]$ tested (Fig. 3c). The generation by OM of a pathway leading to strongly actin-bound motors in parallel with that responsible for the conventional force-generating cycle increases β at sub-saturating $[\text{Ca}^{2+}]$ but not at saturating $[\text{Ca}^{2+}]$ (Fig. 3b). This increase in Ca^{2+} sensitivity, measured by the increase of pCa_{50} by 0.4 units (Table 2), is similar to that reported for demembrated cardiac myocytes^{8,29,30} and is attributable to the contribution of OM-motors to the cooperative effect of attached motors in switching ON the thin filament^{9,45}. The potentiating role of this mechanism in relation to the level of Ca^{2+} is quantified by plotting the difference between T_0 in $1\ \mu\text{M}$ OM and in control (ΔT_0) versus pCa (Fig. 3d): ΔT_0 is negative at saturating and high $[\text{Ca}^{2+}]$ and crosses zero at pCa 6.8 because, at this pCa, the reduced average force per motor ($\sim 1/2$) in $1\ \mu\text{M}$ OM is compensated by the

increased total number of attached motors (\sim twice); at any pCa > 6.8 , $1\ \mu\text{M}$ OM acts as a potentiator increasing the sarcomere force, because the increased Ca -sensitivity makes the total number of motors larger than twice the control. This mechanism applies equally well to explain the OM potentiating effects at the partial Ca^{2+} -activation found in demembrated cardiac myocytes^{8,29,30}. The force-pCa relation in $1\ \mu\text{M}$ OM is characterized not only by the larger Ca -sensitivity but also by a reduced slope: Hill coefficient n is reduced by a factor of 2 (from 2.01 to 0.84, Table 2), in agreement with previous work on both demembrated cardiac myocytes and slow-skeletal muscle fibres^{8,29,30}. The explanation could be related to a negative effect on the cooperativity index of OM-bound motors if the propagation of the activation along the thin filament induced by motor attachment depends on the motor force.

The second mechanism of action of OM, which is revealed in this work, is the recovery from motor force depression with increase in $[\text{Pi}]$ in the range 1–10 mM. This finding per se scales back the relevance of previous mechanisms of action of OM defined in the absence of added Pi, since 1–10 mM is the physiological range of $[\text{Pi}]$ in working muscle. The molecular basis of this mechanism is implicit in the effect of OM on r_{TD} also in the absence of added Pi ($[\text{Pi}] = 1\ \text{mM}$): r_{TD} is depressed by OM with the same dose dependency as T_0 (Fig. 1 c, d), with $[\text{OM}]$ for half-maximum effect $0.5\ \mu\text{M}$, which noteworthy is in the range (0.1–0.6 μM) of the plasma $[\text{OM}]$ in patients under therapeutic treatment^{3,5,46}. This consideration suggests further work in which the mechanism revealed here is tested also for the more clinically competent range of $[\text{OM}]$.

The kinetic model of Fig. 6 is able to fit both T_0 - and r_{TD} -OM relations (continuous lines in Fig. 1 c and d, respectively) assuming that, after Pi release, the OM-bound motor in the $\text{AM}'_{\text{OM}}\text{-ADP}$ state undergoes an isomerization to an $\text{AM}''_{\text{OM}}\text{-ADP}$ state with higher affinity for Pi favouring an “allosteric” exchange Pi-OM (step 14), which allows the motor to re-enter the force-generating cycle. Noteworthy, it is not possible to simulate the depressant effect of OM on r_{TD} confining the allosteric competition between OM and Pi to step 10, because the OM-dependent effect on force would not imply any reduction in r_{TD} . Only introducing the pink-highlighted path that contributes to T_0 with a slower process through the isomerization (step 11) and the following OM-Pi exchange (step 14) the time course of T_0 is slowed and the r_{TD} -Pi relation in $1\ \mu\text{M}$ OM is shifted downward (Fig. 4b). The stoichiometry of the Pi-dependent recovery of the average force per motor in the presence of $1\ \mu\text{M}$ OM (Fig. 4d, open circles) is mainly accounted for by the equilibrium constants of steps 11 (1) and 14 (10^{-3}). For step 14, assuming a second-order rate constant for Pi binding three orders of magnitude smaller than the second-order rate constant for OM binding, the equilibrium is near the unity when the ratio between $[\text{Pi}]$ and $[\text{OM}]$ is about 10^3 (Table 3), that is, with the near millimolar physiological concentration of Pi, at micromolar $[\text{OM}]$.

The energetics of the combined OM-Pi action on contractility has been defined by determining the effect of OM on the rate of ATP hydrolysis (k_{cat}) during isometric contraction at saturating Ca^{2+} and its modulation by Pi. Increase in $[\text{OM}]$ up to $2\ \mu\text{M}$, which decreases T_0 to $1/2$ the control, does not change k_{cat} (Fig. 5b). This result is specific for a loaded contraction, as in both solution^{15,35} and low-load laser trap experiments⁹ on β -cardiac myosin the ATPase rate has been found to be reduced in OM with respect to the control.

In either the pink-highlighted or the conventional green-highlighted path under high load the motors accumulate in the ADP-bound state because either OM (pink path) or the high load (green path) limit the probability to go through the working stroke that would accelerate the next step, the conformation

dependent ADP release^{44,47–49}. Consequently, independent of the reason that limits the execution of the working stroke, both step 12 for OM-bound motors and step 5 for OM-free motors are slow (Table 3) and the ATPase rate is limited in the same way independent of the proportion of motors passing through either path. In this way the model can simulate the OM-dependent drop in T_0 (dashed line in Fig. 5b) without effect on k_{cat} (continuous line).

In the absence of added Pi, OM reduces T_0 through a reduction in F_0 at constant k_{cat} , thus it increases the tension cost (E_T) of the isometric contraction. One micromolar OM, which halves F_0 , doubles E_T (Fig. 5e). Noteworthy, this conclusion extends from maximal contractions at saturating $[\text{Ca}^{2+}]$ to contractions at sub-saturating $[\text{Ca}^{2+}]$ because reduction in $[\text{Ca}^{2+}]$ reduces the total number of attached motors (Fig. 3b) without affecting F_0 (Fig. 3c).

A direct test of Pi effect on OM-bound motors at pCa ~ 7 , where OM exerts its potentiating action via the increase in Ca^{2+} sensitivity (Fig. 3d), would be quite important, considering that the internal $[\text{Ca}^{2+}]$ in the heart systole ranges 0.2–0.6 μM ^{50,51}. However, the sarcomere-level mechanics on isometric contraction of skinned soleus fibres activated at pCa ~ 7 would fail to produce data that can be interpreted in terms of Eq. (1), because the stiffness of the motor array would be too low ($<20 \text{ kPa nm}^{-1}$, Fig. 3b) and the half-sarcomere compliance analysis would be complicated by the significant contribution of the additional elasticity in parallel with the motor array (see “Methods”, Fig. 7b). In this respect it must be noted also that the nature and the effects of the additional parallel elasticity are likely different in the slow-skeletal muscle and in the cardiac muscle, which have different isoforms of the accessory and cytoskeleton proteins like My-BPC and titin. Consequently, the conclusions from soleus muscle could not be directly translated to cardiac muscle as it is instead possible under the condition selected in this study (stiffness of the motor array $> 20 \text{ kPa nm}^{-1}$), in which the half-sarcomere compliance is only determined by the number of β /slow myosin isoforms attached to the actin filament.

Under the conditions defined above, we provide the evidence for a previously unknown inotropic effect on the β /slow MHC isoform in OM-treated myocytes: increase in $[\text{Pi}]$ within the physiological range (1–10 mM) recovers from the inhibitory effect of OM on T_0 by increasing the proportion of motors re-entering the force-generating cycle and this, at constant k_{cat} , implies a corresponding reduction in tension cost (Fig. 5e). This effect of Pi on the OM-bound motors could represent an energetically efficient response in OM-treated cardiomyopathic patients, whenever the increase of heart-beat frequency induces an increase in $[\text{Pi}]$ ^{27,28}.

Methods

Animal and ethical approval. Experiments have been done on demembrated fibres from the soleus muscle of adult male New Zealand white rabbits at either the Physiolab Research Unity of the Biology Department of the University of Florence (mechanical experiments), or the Department of Physiology of the VU University Medical Center in Amsterdam (ATPase rate measurements). The experiments were carried out according to the protocols approved by the Ethical Committee of the University of Florence and by the Italian Ministry of Health (authorization n. 956/2015 PR) in compliance with the Italian regulation on animal experimentation, Decreto Legislativo 26/2014 and the EU regulation (directive 2010/63). Rabbits (4–5 kg weight, 20–30 weeks old) were sacrificed by injection of an overdose of sodium pentobarbitone (150 mg kg⁻¹) in the marginal ear vein. Two rabbits were used for this work. All animals have been kept with free access to food and water prior to use.

Fibre preparation and mechanical apparatus. Small bundles (40–80 fibres) of soleus muscle fibres were stored in skinning solution containing 50% glycerol at -20°C for 3–4 weeks and single fibres were prepared just before the experiment as already described^{18,52}. The osmotic agent Dextran T-500 was added to all solutions at the concentration of 4 g/100 ml (4% weight/volume) that is known to reverse the

permeabilization-induced increase of interfibrillar spacing and cross-sectional area (CSA) to the value before skinning^{18,53–57}.

A fibre segment, 4–6 mm long, was mounted between the lever arms of a loudspeaker motor able to impose steps in length complete within 80 μs and a capacitance force transducer with resonant frequency 40–50 kHz¹⁸. Sarcomere length (sl), width (w) and height (h) of the fibre were measured at 0.5 mm intervals in the 3–4 mm central segment of the relaxed fibre with a 40 \times dry objective (Zeiss, NA 0.60) and a 25 \times eyepiece. The fibre length (L_0) was adjusted to have a sl within the range 2.3–2.5 μm . The fibre CSA was determined assuming the fibre cross-section as elliptical ($\text{CSA} = \pi/4 \cdot w \cdot h$) and its value ranged between 2100 and 5300 μm^2 . Fibres were activated by temperature jump using a solution exchange system¹⁸. The fibre was kept in the activating solution at the test temperature (12 $^\circ\text{C}$) for 4–5 s for the mechanical measurements. A striation follower⁵⁸ allowed nanometre-microsecond resolution recording of length changes in a selected population of sarcomeres (range 500–1200 sarcomeres) starting at the time the optic path was permitted through the glass window in the floor of the test temperature drop (see ref. 18 for details).

Half-sarcomere stiffness measurements. Step length changes (ranging from -2 to $+2 \text{ nm}$ per hs, stretch positive, rise time 100 μs) were imposed on the isometrically contracting fibre to estimate the half-sarcomere stiffness by the slope of the relation between the force attained at the end of the step and the change in half-sarcomere length in the sarcomere population of the segment monitored by the striation follower (T_1 relation) (Figs. 2a, b and 7). To enhance the precision of stiffness measurements, a train of different-sized steps at 200-ms intervals was applied during each activation and, to maintain the isometric force before the test step constant, each test step was followed, after a 50-ms pause, by a step of the same size but opposite direction^{18,19}. Half-sarcomere stiffness measurements were done (i) at different $[\text{OM}]$ (range 0.1–10 μM) in the absence of added Pi (that is with $[\text{Pi}] \sim 1 \text{ mM}$) and with $[\text{Ca}^{2+}]$ for maximum activation (pCa 4.5), (ii) at different $[\text{Ca}^{2+}]$ (range of pCa 4.5–7.5) without and with 1 μM OM and (iii) at different $[\text{Pi}]$ (range 1–20 mM) at pCa 4.5 without and with 1 μM OM.

Half-sarcomere compliance analysis. The elastic characteristics of the array of myosin motors during active isometric contraction can be estimated from the stiffness of the half-sarcomere with a mechanical protocol that allows to isolate and subtract the contribution of the filament compliance (C_f) to half-sarcomere compliance (C_{hs} , which is the reciprocal of the half-sarcomere stiffness k_0). The protocol consists in determining the T_1 relations during activations at different $[\text{Ca}^{2+}]$. In fact, as previously demonstrated¹⁸, $[\text{Ca}^{2+}]$ -dependent changes in maximum isometric force (T_0) are fully accounted for by changes in the number of attached motors. Under this condition the relation between the half-sarcomere strain ($Y_0 = C_{\text{hs}} \cdot T_0$) and T_0 can be interpreted with a simple mechanical model of the half-sarcomere in which the attached motors are represented by an array of in parallel springs, the number of which, but not the strain (s_0), changes in proportion to force, in series with the actin and myosin filaments represented by a spring, which accounts for an equivalent filament compliance (C_f) (Model 1 in ref. 59). According to Model 1, C_{hs} is expressed by the equation⁵⁹:

$$C_{\text{hs}} (= 1/k_0) = C_f + 1/e_0, \quad (1)$$

where $1/e_0$, the compliance of the array of motors, is the reciprocal of the stiffness of the array (e_0 , which is proportional to the number of attached motors). From the above equation the strain of the half-sarcomere $Y_0 (= C_{\text{hs}} \cdot T_0)$ can be derived:

$$Y_0 = (C_{\text{hs}} \cdot T_0 = C_f \cdot T_0 + T_0/e_0) = C_f \cdot T_0 + s_0, \quad (2)$$

where s_0 is the average strain in the attached motors at T_0 . According to the model, Y_0 increases linearly with the force with a slope that is explained by the increase in the strain of the myofilaments with constant compliance C_f , while s_0 , estimated by the ordinate intercept of the $Y_0 - T_0$ relation, is the same independent of T_0 .

The T_1 relations were determined at different pCa in control and in the presence of 1 μM OM (which reduces $T_{0,4.5}$ to $1/2$). Figure 7 shows the relations obtained at pCa 4.5 (circles) and 6.59 (squares) in control (a) and in the presence of 1 μM OM (b). The half-sarcomere stiffness (k_0 , estimated by the slope of the linear fit to data, dashed line) reduces, lowering $[\text{Ca}^{2+}]$, from $28.8 \pm 1.0 \text{ kPa nm}^{-1}$ (filled circles) to $17.1 \pm 0.7 \text{ kPa nm}^{-1}$ (filled squares) in control (a) and from $26.3 \pm 1.5 \text{ kPa nm}^{-1}$ (open circles) to $20.9 \pm 0.9 \text{ kPa nm}^{-1}$ (open squares) in the presence of OM (b). In both conditions the half-sarcomere strain at T_0 (Y_0 , estimated by the extrapolation of the fit to zero force) is shifted rightward with lowering $[\text{Ca}^{2+}]$, but less than in proportion to the reduction of the ordinate intercept, in agreement with the reduction of k_0 . In Fig. 7c, Y_0 at different $[\text{Ca}^{2+}]$ in control (filled circles) and in the presence of 1 μM OM (open circles) is plotted against the corresponding T_0 . In control, Y_0 increases linearly with the isometric force, with the exception of the lowest points (for $T_0 < 50 \text{ kPa}$) that are shifted downward. The linear relation is expected from Model 1 and the deviation from linearity at very low forces has been explained with the presence of an elastic element in parallel with the myosin motors with a stiffness that is so small that it affects the linear relation only in the region where the number of the motors, and thus their cumulative stiffness are quite low⁵⁹. Noteworthy, the $Y_0 - T_0$ relation in OM (open circles in Fig. 7c) does not show deviation from linearity (see below for the explanation). The values of C_f and s_0 , estimated by fitting Equation (2) to $Y_0 - T_0$ values in control (in the range

of $T_0 > 50$ kPa) and in the presence of OM are reported in Table 1. The value of C_f in the presence of OM (15.3 nm MPa^{-1}) does not differ significantly from the control value (15.2 nm MPa^{-1} , $P > 0.9$, Student's t test), indicating that also in this case the dependence of T_0 on $[\text{Ca}^{2+}]$ is explained by the Ca^{2+} -modulation of the number of attached motors without change in motor strain.

In OM the $Y_0 - T_0$ relation (open circles in Fig. 7c) does not show deviation from linearity for the same low forces at which the control relation shows a downward shift. This apparent contradiction is explained by considering the effect of OM that reduces the force per motor but increases the Ca-sensitivity for motor attachment, so that at the same low values of T_0 , in the presence of OM, the number of attached motors and thus their cumulative stiffness are higher than in control and still in the range of values that mask the contribution of the parallel elastic element. A quantitative evaluation of this interpretation is obtained in Fig. 7d by plotting Y_0 versus the stiffness of the array of motors e_0 at each pCa (data from Fig. 3b) for both control (filled circles) and OM (open circles). It can be seen that both control and OM relations are almost linear in the same range of e_0 , where the stiffness of attached motors is high enough to mask the contribution of the parallel elastic element, and that the control relation deviates from linearity, uncovering the presence of a parallel elastic element, for the small e_0 values that are not attained by the OM relation.

ATPase measurements. Fibre bundles prepared in Florence lab as described above were transported to Amsterdam in ice-cold relaxing solution. ATPase activity (temperature 12°C) at saturating $[\text{Ca}^{2+}]$ and at different $[\text{Pi}]$ was measured photometrically by enzymatic coupling of the regeneration of ATP to the oxidation of NADH present in the bathing solution^{36,60,61} both in control and in the presence of OM (1 and $2 \mu\text{M}$). NADH breakdown was monitored via the absorption of near UV light at 340 nm . Briefly, the set up consisted of two anodized aluminium troughs (volume $80 \mu\text{l}$ each) containing relaxing and pre-activating solution and a measuring chamber (volume about $30 \mu\text{l}$) containing activating solution. The solution was continuously stirred via a membrane at the base of the chamber. UV light passed through the chamber beneath the fibre, and the transmitted light was monitored by two UV-enhanced photodiodes at 340 and 400 nm . The photodiode at 400 nm provided a reference signal, independent of NADH concentration. A syringe, controlled by a stepper motor, was used to add $0.05 \mu\text{l}$ of 10 mM ADP at the end of each recording to calibrate the absorbance signal. Force during the enzymatic assay was measured by means of a strain gauge transducer (AE801 SensoNor, Horten, Norway). The force and the absorbance signals were filtered at 1 kHz and 2.5 Hz , respectively. The ATPase rate was measured as the slope over time of the absorbance signal.

Procedure for the selection of the parameters of the kinetic model. The procedure followed to assign a specific value to the kinetic parameters concerning the effects of OM and Pi on the force (T_0), rate of force development (r_{TD}), stiffness of the motor array (e_0) and ATPase rate (k_{cat}) (eight relations altogether) is based on an iterative routine in which the values of the rate constants (or equilibrium constants) controlling the kinetics of the relevant steps (8–12 and 14) are changed one at a time. For each value of the rate/equilibrium constant (k) the weighted mean of residual errors for each relation is calculated according to the expression:

$$R_w(k) = \frac{1}{N} \sum_{i=1}^N \frac{(x_i - x_{\text{mod}}(k)_i)^2}{x_i^2},$$

where $R_w(k)$ is the mean sum of residuals (weighted for the squared value of the experimental point to allow homogeneous comparison among the eight different relations), x_i is the experimental point value, $x_{\text{mod}}(k)_i$ is the corresponding simulated value for a given k , and N is the number of points in each relation.

An example of the selection procedure for a given rate constant (k_{+14}) in relation to its effect on each of the eight relevant relations is given in Supplementary Fig. 2, where in the left column six simulations obtained for different values of k_{+14} (each identified by a different colour) of four of the eight relations are superimposed on the experimental relations (open symbols) and, in the right column, the weighted mean of residuals (R_w) are plotted versus the value of k_{+14} assumed in each simulation (identified by the same colour as in the left column). As shown by the plots in the right column of Supplementary Fig. 2, the sensitivity of the test in showing a minimum mean residual and its dependence on the value of the rate/equilibrium constant varies depending on the relation. For this, the criterion of selection of the best value for any given rate/equilibrium constant is based on the minimization of the weighted mean of the residuals averaged over the eight relations (global mean, $\langle R_w(k) \rangle$):

$$\langle R_w(k) \rangle = \frac{1}{8} \sum_{p=1}^8 R_w(k).$$

In Supplementary Fig. 3 the values of $\langle R_w(k) \rangle$ are plotted versus the rate/equilibrium constant under consideration. The value selected with this global fitting for each rate/equilibrium constant, identified by the abscissa of the filled symbol, is reported in Table 3.

Solutions. The composition of the solutions, similar for the mechanical and the ATPase measurements (MgATP , 5 mM ; free Mg^{2+} , 1.2 mM) is reported in Supplementary Table 2. The activating solution at a given pCa (range 7.5 – 4.5) was obtained by mixing relaxing and activating solutions. OM (CK-1827452 from Selleckchem, USA) was dissolved in DMSO (Sigma D-5879) (stock solution, 17.5 mM). Different OM concentrations in the final solutions (0.1 – $10 \mu\text{M}$ range) were obtained for partial dilution starting from the stock solution. Four percent dextran was added to all solutions for the mechanical experiments.

Statistical analysis. All data were analyzed using dedicated programs written in LabVIEW (National Instruments) and Microsoft Excel and Origin 2018 (OriginLab Corp., Northampton, MA, USA) software. Error bars on mean data points are $\pm\text{SEM}$.

For mean data in the figures and tables, the number of fibres is reported in the legends and the number of observations, which may vary for each data point, can be recovered from the Source Data files.

Reporting summary. Further information on research design is available in the Nature Research Reporting Summary linked to this article.

Data availability

The authors declare that the data supporting the findings of this study are available within the paper and its Supplementary Information files. The source data for Figs. 1, 2, 3, 4, 5, 7, Supplementary Figs. 1, 2 and 3 and for Tables 1, 2 and Supplementary Table 1 are provided as a Source Data file. All remaining data will be available from the corresponding author upon reasonable request. Source data are provided with this paper.

Received: 25 September 2019; Accepted: 26 May 2020;

Published online: 07 July 2020

References

- Spudich, J. A. Hypertrophic and dilated cardiomyopathy: four decades of basic research on muscle lead to potential therapeutic approaches to these devastating genetic diseases. *Biophys. J.* **106**, 1236–1249 (2014).
- Malik, F. I. et al. Cardiac myosin activation: a potential therapeutic approach for systolic heart failure. *Science* **331**, 1439–1443 (2011).
- Cleland, J. G. et al. The effects of the cardiac myosin activator, omecamtiv mecarbil, on cardiac function in systolic heart failure: a double-blind, placebo-controlled, crossover, dose-ranging phase 2 trial. *Lancet* **378**, 676–683 (2011).
- Teerlink, J. R. et al. Dose-dependent augmentation of cardiac systolic function with the selective cardiac myosin activator, omecamtiv mecarbil: a first-in-man study. *Lancet* **378**, 667–675 (2011).
- Teerlink, J. R. et al. Acute treatment with omecamtiv mecarbil to increase contractility in acute heart failure: The ATOMIC-AHF Study. *J. Am. Coll. Cardiol.* **67**, 1444–1455 (2016).
- Morgan, B. P. et al. Discovery of omecamtiv mecarbil the first, selective, small molecule activator of cardiac Myosin. *ACS Med. Chem. Lett.* **1**, 472–477 (2010).
- Kaplinsky, E. & Mallarkey, G. Cardiac myosin activators for heart failure therapy: focus on omecamtiv mecarbil. *Drugs Context* **7**, 212518 (2018).
- Nagy, L. et al. The novel cardiac myosin activator omecamtiv mecarbil increases the calcium sensitivity of force production in isolated cardiomyocytes and skeletal muscle fibres of the rat. *Br. J. Pharmacol.* **172**, 4506–4518 (2015).
- Woody, M. S. et al. Positive cardiac inotrope omecamtiv mecarbil activates muscle despite suppressing the myosin working stroke. *Nat. Commun.* **9**, 3838 (2018).
- Schiaffino, S. & Reggiani, C. Molecular diversity of myofibrillar proteins: gene regulation and functional significance. *Physiol. Rev.* **76**, 371–423 (1996).
- van Rooij, E. et al. A family of microRNAs encoded by myosin genes governs myosin expression and muscle performance. *Developmental Cell* **17**, 662–673 (2009).
- Chikuni, K., Muroya, S., Tanabe R-i & Nakajima, I. Comparative sequence analysis of four myosin heavy chain isoforms expressed in porcine skeletal muscles: Sequencing and characterization of the porcine myosin heavy chain slow isoform. *Anim. Sci. J.* **73**, 257–262 (2002).
- Rohde, J. A., Thomas, D. D. & Muretta, J. M. Heart failure drug changes the mechanoenzymology of the cardiac myosin powerstroke. *Proc. Natl Acad. Sci. USA* **114**, E1796–E1804 (2017).
- Planelles-Herrero, V. J., Hartman, J. J., Robert-Paganin, J., Malik, F. I. & Houdusse, A. Mechanistic and structural basis for activation of cardiac myosin force production by omecamtiv mecarbil. *Nat. Commun.* **8**, 190 (2017).
- Liu, Y., White, H. D., Belknap, B., Winkelmann, D. A. & Forgacs, E. Omecamtiv Mecarbil modulates the kinetic and motile properties of porcine beta-cardiac myosin. *Biochemistry* **54**, 1963–1975 (2015).

16. Aksel, T., Choe, Yu. E., Sutton, S., Ruppel, K. M. & Spudich, J. A. Ensemble force changes that result from human cardiac myosin mutations and a small-molecule effector. *Cell Rep.* **11**, 910–920 (2015).
17. Winkelmann, D. A., Forgacs, E., Miller, M. T. & Stock, A. M. Structural basis for drug-induced allosteric changes to human beta-cardiac myosin motor activity. *Nat. Commun.* **6**, 7974 (2015).
18. Linari, M., Caremani, M., Piperio, C., Brandt, P. & Lombardi, V. Stiffness and fraction of Myosin motors responsible for active force in permeabilized muscle fibers from rabbit psoas. *Biophys. J.* **92**, 2476–2490 (2007).
19. Percario, V. et al. Mechanical parameters of the molecular motor myosin II determined in permeabilized fibres from slow and fast skeletal muscles of the rabbit. *J. Physiol.* **596**, 1243–1257 (2018).
20. Caremani, M. et al. Size and speed of the working stroke of cardiac myosin in situ. *Proc. Natl Acad. Sci. USA* **113**, 3675–3680 (2016).
21. Pinzauti, F. et al. The force and stiffness of myosin motors in the isometric twitch of a cardiac trabecula and the effect of the extracellular calcium concentration. *J. Physiol.* **596**, 2581–2596 (2018).
22. Allen, D. G., Morris, P. G., Orchard, C. H. & Pirollo, J. S. A nuclear magnetic resonance study of metabolism in the ferret heart during hypoxia and inhibition of glycolysis. *J. Physiol.* **361**, 185–204 (1985).
23. Kentish, J. C. The effects of inorganic phosphate and creatine phosphate on force production in skinned muscles from rat ventricle. *J. Physiol.* **370**, 585–604 (1986).
24. Morris P. G., Allen D. G. & Orchard C. H. High-time-resolution 31P NMR studies of the perfused ferret heart. In: *Advances in Myocardiology* (eds Harris, P. & Poole-Wilson, P.A.) (Springer US, 1985).
25. Meyer, R. A., Brown, T. R. & Kushmerick, M. J. Phosphorus nuclear magnetic resonance of fast- and slow-twitch muscle. *Am. J. Physiol.* **248**, C279–C287 (1985).
26. Bevington, A. et al. A study of intracellular orthophosphate concentration in human muscle and erythrocytes by 31P nuclear magnetic resonance spectroscopy and selective chemical assay. *Clin. Sci.* **71**, 729–735 (1986).
27. Elliott, A. C., Smith, G. L. & Allen, D. G. The metabolic consequences of an increase in the frequency of stimulation in isolated ferret hearts. *J. Physiol.* **474**, 147–159 (1994).
28. Eijgelshoven, M. H. et al. Cardiac high-energy phosphates adapt faster than oxygen consumption to changes in heart rate. *Circ. Res.* **75**, 751–759 (1994).
29. Kampourakis, T., Zhang, X., Sun, Y. B. & Irving, M. Omecamtiv mecarbil and blebbistatin modulate cardiac contractility by perturbing the regulatory state of the myosin filament. *J. Physiol.* **596**, 31–46 (2018).
30. Kieu, T. T., Awinda, P. O. & Tanner, B. C. W. Omecamtiv mecarbil slows myosin kinetics in skinned rat myocardium at physiological temperature. *Biophys. J.* **116**, 2149–2160 (2019).
31. Pate, E. & Cooke, R. A model of crossbridge action: the effects of ATP, ADP and Pi. *J. Muscle Res. Cell Motil.* **10**, 181–196 (1989).
32. Millar, N. C. & Homsher, E. Kinetics of force generation and phosphate release in skinned rabbit soleus muscle fibers. *Am. J. Physiol.* **262**, C1239–C1245 (1992).
33. Tesi, C., Colomo, F., Piroddi, N. & Poggesi, C. Characterization of the cross-bridge force-generating step using inorganic phosphate and BDM in myofibrils from rabbit skeletal muscles. *J. Physiol.* **541**, 187–199 (2002).
34. Caremani, M., Dantzig, J., Goldman, Y. E., Lombardi, V. & Linari, M. Effect of inorganic phosphate on the force and number of myosin cross-bridges during the isometric contraction of permeabilized muscle fibers from rabbit psoas. *Biophys. J.* **95**, 5798–5808 (2008).
35. Swenson, A. M. et al. Omecamtiv mecarbil enhances the duty ratio of human beta-cardiac myosin resulting in increased calcium sensitivity and slowed force development in cardiac muscle. *J. Biol. Chem.* **292**, 3768–3778 (2017).
36. Potma, E. J., van Graas, I. A. & Stienen, G. J. Effects of pH on myofibrillar ATPase activity in fast and slow skeletal muscle fibers of the rabbit. *Biophys. J.* **67**, 2404–2410 (1994).
37. Linari, M., Caremani, M. & Lombardi, V. A kinetic model that explains the effect of inorganic phosphate on the mechanics and energetics of isometric contraction of fast skeletal muscle. *Proc. Biol. Sci.* **277**, 19–27 (2010).
38. Johnson, C. A. et al. The ATPase cycle of human muscle myosin II isoforms: Adaptation of a single mechanochemical cycle for different physiological roles. *J. Biol. Chem.* **294**, 14267–14278 (2019).
39. Potma, E. J., van Graas, I. A. & Stienen, G. J. Influence of inorganic phosphate and pH on ATP utilization in fast and slow skeletal muscle fibers. *Biophys. J.* **69**, 2580–2589 (1995).
40. Bowater, R. & Sleep, J. Demembrated muscle fibers catalyze a more rapid exchange between phosphate and adenosine triphosphate than actomyosin subfragment 1. *Biochemistry* **27**, 5314–5323 (1988).
41. Millar, N. C. & Homsher, E. The effect of phosphate and calcium on force generation in glycerinated rabbit skeletal muscle fibers. A steady-state and transient kinetic study. *J. Biol. Chem.* **265**, 20234–20240 (1990).
42. Dantzig, J. A., Goldman, Y. E., Millar, N. C., Laktis, J. & Homsher, E. Reversal of the cross-bridge force-generating transition by photogeneration of phosphate in rabbit psoas muscle fibres. *J. Physiol.* **451**, 247–278 (1992).
43. Caremani, M., Melli, L., Dolfi, M., Lombardi, V. & Linari, M. The working stroke of the myosin II motor in muscle is not tightly coupled to release of orthophosphate from its active site. *J. Physiol.* **591**, 5187–5205 (2013).
44. Caremani, M., Melli, L., Dolfi, M., Lombardi, V. & Linari, M. Force and number of myosin motors during muscle shortening and the coupling with the release of the ATP hydrolysis products. *J. Physiol.* **593**, 3313–3332 (2015).
45. McKillop, D. F. & Geeves, M. A. Regulation of the interaction between actin and myosin subfragment 1: evidence for three states of the thin filament. *Biophys. J.* **65**, 693–701 (1993).
46. Vu, T. et al. Population pharmacokinetic-pharmacodynamic modeling of omecamtiv mecarbil, a cardiac myosin activator, in healthy volunteers and patients with stable heart failure. *J. Clin. Pharmacol.* **55**, 1236–1247 (2015).
47. Dantzig, J. A., Hibberd, M. G., Trentham, D. R. & Goldman, Y. E. Cross-bridge kinetics in the presence of MgADP investigated by photolysis of caged ATP in rabbit psoas muscle fibres. *J. Physiol.* **432**, 639–680 (1991).
48. Siemankowski, R. F., Wiseman, M. O. & White, H. D. ADP dissociation from actomyosin subfragment 1 is sufficiently slow to limit the unloaded shortening velocity in vertebrate muscle. *Proc. Natl Acad. Sci. USA* **82**, 658–662 (1985).
49. Potma, E. J. & Stienen, G. J. Increase in ATP consumption during shortening in skinned fibres from rabbit psoas muscle: effects of inorganic phosphate. *J. Physiol.* **496**(Pt 1), 1–12 (1996).
50. Gao, W. D., Atar, D., Backx, P. H. & Marban, E. Relationship between intracellular calcium and contractile force in stunned myocardium. Direct evidence for decreased myofilament Ca²⁺ responsiveness and altered diastolic function in intact ventricular muscle. *Circ. Res.* **76**, 1036–1048 (1995).
51. Frampton, J. E., Orchard, C. H. & Boyett, M. R. Diastolic, systolic and sarcoplasmic reticulum [Ca²⁺] during inotropic interventions in isolated rat myocytes. *J. Physiol.* **437**, 351–375 (1991).
52. Goldman, Y. E., Hibberd, M. G. & Trentham, D. R. Relaxation of rabbit psoas muscle fibres from rigor by photochemical generation of adenosine-5'-triphosphate. *J. Physiol.* **354**, 577–604 (1984).
53. Brenner, B. & Yu, L. C. Characterization of radial force and radial stiffness in Ca(2+)-activated skinned fibres of the rabbit psoas muscle. *J. Physiol.* **441**, 703–718 (1991).
54. Kawai, M., Wray, J. S. & Zhao, Y. The effect of lattice spacing change on cross-bridge kinetics in chemically skinned rabbit psoas muscle fibers. I. Proportionality between the lattice spacing and the fiber width. *Biophys. J.* **64**, 187–196 (1993).
55. Matsubara, I. & Elliott, G. F. X-ray diffraction studies on skinned single fibres of frog skeletal muscle. *J. Mol. Biol.* **72**, 657–669 (1972).
56. Maughan, D. W. & Godt, R. E. Stretch and radial compression studies on relaxed skinned muscle fibers of the frog. *Biophys. J.* **28**, 391–402 (1979).
57. Linari, M. et al. The stiffness of skeletal muscle in isometric contraction and rigor: the fraction of myosin heads bound to actin. *Biophys. J.* **74**, 2459–2473 (1998).
58. Huxley, A. F., Lombardi, V. & Peachey, D. A system for fast recording of longitudinal displacement of a striated muscle fibre. *J. Physiol.* **317**, 12–13 (1981).
59. Fusi, L., Brunello, E., Reconditi, M., Piazzesi, G. & Lombardi, V. The non-linear elasticity of the muscle sarcomere and the compliance of myosin motors. *J. Physiol.* **592**, 1109–1118 (2014).
60. Glyn, H. & Sleep, J. Dependence of adenosine triphosphatase activity of rabbit psoas muscle fibres and myofibrils on substrate concentration. *J. Physiol.* **365**, 259–276 (1985).
61. Potma, E. J., Stienen, G. J., Barends, J. P. & Elzinga, G. Myofibrillar ATPase activity and mechanical performance of skinned fibres from rabbit psoas muscle. *J. Physiol.* **474**, 303–317 (1994).
62. White, H. D. & Taylor, E. W. Energetics and mechanism of actomyosin adenosine triphosphatase. *Biochemistry* **15**, 5818–5826 (1976).
63. Sleep, J. A. & Taylor, E. W. Intermediate states of actomyosin adenosine triphosphatase. *Biochemistry* **15**, 5813–5817 (1976).
64. Goldman, Y. E. Kinetics of the actomyosin ATPase in muscle fibers. *Annu Rev. Physiol.* **49**, 637–654 (1987).
65. Kawai, M. & Halvorson, H. R. Two step mechanism of phosphate release and the mechanism of force generation in chemically skinned fibers of rabbit psoas muscle. *Biophys. J.* **59**, 329–342 (1991).
66. Nyitrai, M. & Geeves, M. A. Adenosine diphosphate and strain sensitivity in myosin motors. *Philos. Trans. R. Soc. Lond. B Biol. Sci.* **359**, 1867–1877 (2004).

Acknowledgements

We thank Massimo Reconditi for insightful comments on the manuscript and valuable support to the definition of the procedure for the optimization of the simulation and the staff of the mechanical workshop of the Department of Physics and Astronomy (University of Florence) for mechanical engineering support. This work was supported by the University of Florence and Fondazione Cassa di Risparmio di Firenze (Italy).

Author contributions

V.L., M.L., G.P., M.C., C.O. and G.S. designed the research. S.G., M.C. and I.P. performed the experiments and analysed the data. V.L., M.L. and G.P. wrote the paper or revised it critically for important intellectual content. All authors participated in discussions on this work and approved the final version of the manuscript.

Competing interests

The authors declare no competing interests.

Additional information

Supplementary information is available for this paper at <https://doi.org/10.1038/s41467-020-17143-2>.

Correspondence and requests for materials should be addressed to V.L.

Peer review information *Nature Communications* thanks Anne Houdusse, and other, anonymous, reviewer(s) for their contribution to the peer review of this work. Peer reviewer reports are available.

Reprints and permission information is available at <http://www.nature.com/reprints>

Publisher's note Springer Nature remains neutral with regard to jurisdictional claims in published maps and institutional affiliations.



Open Access This article is licensed under a Creative Commons Attribution 4.0 International License, which permits use, sharing, adaptation, distribution and reproduction in any medium or format, as long as you give appropriate credit to the original author(s) and the source, provide a link to the Creative Commons license, and indicate if changes were made. The images or other third party material in this article are included in the article's Creative Commons license, unless indicated otherwise in a credit line to the material. If material is not included in the article's Creative Commons license and your intended use is not permitted by statutory regulation or exceeds the permitted use, you will need to obtain permission directly from the copyright holder. To view a copy of this license, visit <http://creativecommons.org/licenses/by/4.0/>.

© The Author(s) 2020